Supplementary Information for

Three-dimensional non-Abelian Bloch oscillations and novel higher-order topological states

Naiqiao Pan*, Tian Chen*, Tingting Ji, Xiaoxue Tong and Xiangdong Zhang+

Key Laboratory of advanced optoelectronic quantum architecture and measurements of Ministry of Education, Beijing Key Laboratory of Nanophotonics & Ultrafine Optoelectronic Systems, School of Physics, Beijing Institute of Technology, 100081, Beijing, China

**These authors contributed equally to this work. +$Author to whom any correspondence should be addressed. E-mail: zhangxd@bit.edu.cn, chentian@bit.edu.cn*

Supplementary Note 1. Wilson line matrix and winding number.

Supplementary Note 2. The synchronization between real-space motion and band-population dynamics.

Supplementary Note 3. The influence of non-abelian Berry curvature on real-space dynamics.

Supplementary Note 4. Results of the dynamics in paths $\mathbb{C}_2$, $\mathbb{C}_3$, and $\mathbb{C}_4$.

Supplementary Note 5. Details for the Experimental realization of 3D non-Abelian BOs.

Supplementary Note 6. The influence of disorder effects on the Bloch oscillations in circuit simulators.

Supplementary Note 7. Topologically protected 2D surface states.

Supplementary Note 8. The proof for the topological properties of novel higher-order 1D boundary states.

Supplementary Note 9. Designed circuits for the topologically protected 1D boundary states.

Supplementary Note 1. Wilson line matrix and winding number.

The Hamiltonian of the 3D HOTI model can be written in the chiral-symmetric form as

$$H(\mathbf{k}) = \sum_{i=1}^{6} d_i(\mathbf{k})\Gamma_i' = \begin{pmatrix} 0 & Q(\mathbf{k}) \\ Q^{\dagger}(\mathbf{k}) & 0 \end{pmatrix}, \tag{1}$$

where

$$Q(\mathbf{k}) = i\sum_{i=1}^{5} d_i(\mathbf{k})\Gamma_i - d_6(\mathbf{k})I_4. \tag{2}$$

The two fourfold degenerate energy bands can be expressed as $\pm\varepsilon = \pm\sqrt{d_1^2 + d_2^2 + d_3^2 + d_4^2 + d_5^2 + d_6^2}$. It should be noticed that $Q^{\dagger} = \varepsilon^2 Q^{-1}$.

The lowest four eigenstates can be written as

$$\begin{aligned}
\left|\psi_k^1\right\rangle &= \frac{1}{\sqrt{2\varepsilon}}\left(0, id_3 - d_4, -id_1 - d_2, -id_5 + d_6, 0, 0, 0, E\right)^T, \\
\left|\psi_k^2\right\rangle &= \frac{1}{\sqrt{2\varepsilon}}\left(-id_3 + d_4, 0, id_5 + d_6, -id_1 + d_2, 0, 0, E, 0\right)^T, \\
\left|\psi_k^3\right\rangle &= \frac{1}{\sqrt{2\varepsilon}}\left(-id_1 - d_2, id_5 + d_6, 0, id_3 + d_4, 0, E, 0, 0\right)^T, \\
\left|\psi_k^4\right\rangle &= \frac{1}{\sqrt{2\varepsilon}}\left(-id_5 + d_6, -id_1 + d_2, -id_3 - d_4, 0, E, 0, 0, 0\right)^T.
\end{aligned} \tag{3}$$

Now we focus on the 2π/3 rotation symmetries whose axes are along the four paths defined in the main text. Here, we assume that each d_i function only depends on one component of the momentum k, namely $d_1 = d_1(k_y)$, $d_2 = d_2(k_y)$, $d_3 = d_3(k_x)$, $d_4 = d_4(k_x)$, $d_5 = d_5(k_z)$, and $d_6 = d_6(k_z)$, which is satisfied by the 3D HOTI model.

First, we study the 2π/3 rotation symmetry axes $\mathbb{C}_1$ pointing along the sites 3 and 6, which is illustrated in Fig. S1. The corresponding symmetry operator $\widehat{C}_{3,1}$ has the function as $\widehat{C}_{3,1}H\left(k_x, k_y, k_z\right)\widehat{C}_{3,1}^{-1} = H\left(k_y, k_z, k_x\right)$. This symmetry is satisfied if and only if

$$
\begin{aligned}
d_1\left(k_x,k_y,k_z\right) &\overset{\hat{C}_{3,1}}{=} d_3\left(k_y,k_z,k_x\right),\\
d_2\left(k_x,k_y,k_z\right) &\overset{\hat{C}_{3,1}}{=} d_4\left(k_y,k_z,k_x\right),\\
d_3\left(k_x,k_y,k_z\right) &\overset{\hat{C}_{3,1}}{=} d_5\left(k_y,k_z,k_x\right),\\
d_4\left(k_x,k_y,k_z\right) &\overset{\hat{C}_{3,1}}{=} d_6\left(k_y,k_z,k_x\right),\\
d_5\left(k_x,k_y,k_z\right) &\overset{\hat{C}_{3,1}}{=} d_1\left(k_y,k_z,k_x\right),\\
d_6\left(k_x,k_y,k_z\right) &\overset{\hat{C}_{3,1}}{=} d_2\left(k_y,k_z,k_x\right),
\end{aligned}
\tag{4}
$$

where

$$
\hat{C}_{3,1} = \begin{pmatrix}
0 & -1 & 0 & 0 & 0 & 0 & 0 & 0\\
0 & 0 & 0 & 1 & 0 & 0 & 0 & 0\\
0 & 0 & 1 & 0 & 0 & 0 & 0 & 0\\
-1 & 0 & 0 & 0 & 0 & 0 & 0 & 0\\
0 & 0 & 0 & 0 & 0 & 0 & 0 & 1\\
0 & 0 & 0 & 0 & 0 & 1 & 0 & 0\\
0 & 0 & 0 & 0 & -1 & 0 & 0 & 0\\
0 & 0 & 0 & 0 & 0 & 0 & -1 & 0
\end{pmatrix}.
$$

Now we define the winding number along the closed path $\mathbb{C}_1$ as

$$
\begin{aligned}
w_1 &= \frac{i}{4\pi}\int_{\mathbb{C}_1} \mathrm{d}\mathbf{k}\cdot \mathrm{Tr}[Q^{-1}(\mathbf{k})D_1\partial_{\mathbf{k}}Q(\mathbf{k})]\\
&= \frac{i}{4\pi}\int_{\mathbb{C}_1} \mathrm{d}\mathbf{k}\cdot \frac{-4i(d_1\partial_{\mathbf{k}}d_2 - d_2\partial_{\mathbf{k}}d_1 + d_3\partial_{\mathbf{k}}d_4 - d_4\partial_{\mathbf{k}}d_3 + d_5\partial_{\mathbf{k}}d_6 - d_6\partial_{\mathbf{k}}d_5)}{\varepsilon^2},
\end{aligned}
\tag{5}
$$

where

$$
D_1 = \begin{pmatrix}
-1 & 0 & 0 & 0\\
0 & -1 & 0 & 0\\
0 & 0 & 3 & 0\\
0 & 0 & 0 & -1
\end{pmatrix}.
$$

Notice that along the path $\mathbb{C}_1$, there is $k_x = k_y = k_z$, which constrains the vectors d_i respecting (4) as $d_1 = d_3 = d_5$ and $d_2 = d_4 = d_6$. Then we have

$$
w_1 = \frac{1}{\pi}\int_0^{2\pi} \mathrm{d}k\, \frac{d_1\partial_k d_2 - d_2\partial_k d_1}{|d_1|^2 + |d_2|^2}, \tag{6}
$$

which corresponds to the main text.

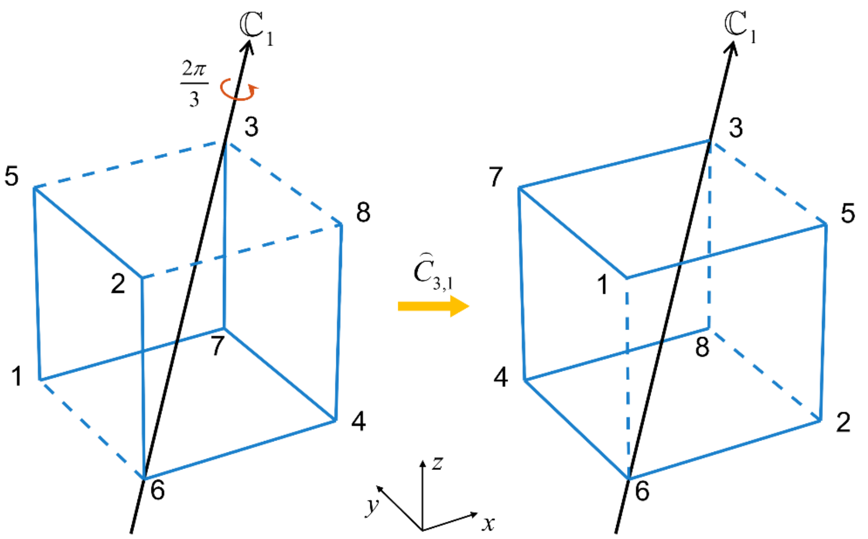

Figure S1. The 2π/3 rotation symmetry in the 3D lattices. The schematic diagram for the 2π/3 rotation symmetry $\hat{C}_{3,1}$, whose symmetry axis is along the path $\mathbb{C}_1$. Under the requirement of $\hat{C}_{3,1}$, the Hamiltonian satisfies $\hat{C}_{3,1}H\left(k_x,k_y,k_z\right)\hat{C}_{3,1}^{-1}=H\left(k_y,k_z,k_x\right)$.

The same conclusion can also be obtained in paths $\mathbb{C}_2$, $\mathbb{C}_3$, and $\mathbb{C}_4$. For the 2π/3 rotation symmetry axes $\mathbb{C}_2$ pointing along the sites 4 and 5, the corresponding 2π/3 rotation symmetry operator $\hat{C}_{3,2}H\left(k_x,k_y,k_z\right)\hat{C}_{3,2}^{-1}=H\left(-k_z,-k_x,k_y\right)$, which is satisfied when

$$
\begin{aligned}
d_1\left(k_x,k_y,k_z\right) &\overset{\hat{C}_{3,2}}{=} d_5\left(-k_z,-k_x,k_y\right),\\
d_2\left(k_x,k_y,k_z\right) &\overset{\hat{C}_{3,2}}{=} d_6\left(-k_z,-k_x,k_y\right),\\
d_3\left(k_x,k_y,k_z\right) &\overset{\hat{C}_{3,2}}{=} -d_1\left(-k_z,-k_x,k_y\right),\\
d_4\left(k_x,k_y,k_z\right) &\overset{\hat{C}_{3,2}}{=} d_2\left(-k_z,-k_x,k_y\right),\\
d_5\left(k_x,k_y,k_z\right) &\overset{\hat{C}_{3,2}}{=} -d_3\left(-k_z,-k_x,k_y\right),\\
d_6\left(k_x,k_y,k_z\right) &\overset{\hat{C}_{3,2}}{=} d_4\left(-k_z,-k_x,k_y\right),
\end{aligned}
$$

where

$$
\hat{C}_{3,2} = \begin{pmatrix} 0 & 1 & 0 & 0 & 0 & 0 & 0 & 0 \\ 0 & 0 & -1 & 0 & 0 & 0 & 0 & 0 \\ -1 & 0 & 0 & 0 & 0 & 0 & 0 & 0 \\ 0 & 0 & 0 & 1 & 0 & 0 & 0 & 0 \\ 0 & 0 & 0 & 0 & 1 & 0 & 0 & 0 \\ 0 & 0 & 0 & 0 & 0 & 0 & 0 & 1 \\ 0 & 0 & 0 & 0 & 0 & 1 & 0 & 0 \\ 0 & 0 & 0 & 0 & 0 & 0 & 1 & 0 \end{pmatrix}.
$$

We then define

$$
w_2 = \frac{i}{4\pi}\int_{\mathbb{C}_2} \mathrm{d}\mathbf{k}\cdot \mathrm{Tr}[Q^{-1}(\mathbf{k})D_2\partial_{\mathbf{k}}Q(\mathbf{k})] = \frac{1}{\pi}\int_0^{2\pi} \mathrm{d}k\, \frac{d_1\partial_k d_2 - d_2\partial_k d_1}{|d_1|^2+|d_2|^2}, \tag{7}
$$

with $D_2 = \begin{pmatrix} 1 & 0 & 0 & 0 \\ 0 & 1 & 0 & 0 \\ 0 & 0 & 1 & 0 \\ 0 & 0 & 0 & -3 \end{pmatrix}$. It is required that $d_1 = -d_3 = d_5$ and $d_2 = d_4 = d_6$ when $-k_x = k_y = k_z$. For the 2π/3 rotation symmetry axes $\mathbb{C}_3$ pointing along the sites 1 and 8, the corresponding 2π/3 rotation symmetry operator $\hat{C}_{3,3}$ leads to $\hat{C}_{3,3}H(k_x,k_y,k_z)\hat{C}_{3,3}^{-1} = H(k_z,-k_x,-k_y)$, which is satisfied when

$$
\begin{aligned}
d_1(k_x,k_y,k_z) &\overset{\hat{C}_{3,3}}{=} -d_5(k_z,-k_x,-k_y), \\
d_2(k_x,k_y,k_z) &\overset{\hat{C}_{3,3}}{=} d_6(k_z,-k_x,-k_y), \\
d_3(k_x,k_y,k_z) &\overset{\hat{C}_{3,3}}{=} -d_1(k_z,-k_x,-k_y), \\
d_4(k_x,k_y,k_z) &\overset{\hat{C}_{3,3}}{=} d_2(k_z,-k_x,-k_y), \\
d_5(k_x,k_y,k_z) &\overset{\hat{C}_{3,3}}{=} d_3(k_z,-k_x,-k_y), \\
d_6(k_x,k_y,k_z) &\overset{\hat{C}_{3,3}}{=} d_4(k_z,-k_x,-k_y),
\end{aligned}
$$

where

$$\hat{C}_{3,3}=\begin{pmatrix} -1 & 0 & 0 & 0 & 0 & 0 & 0 & 0 \\ 0 & 0 & 0 & 1 & 0 & 0 & 0 & 0 \\ 0 & -1 & 0 & 0 & 0 & 0 & 0 & 0 \\ 0 & 0 & 1 & 0 & 0 & 0 & 0 & 0 \\ 0 & 0 & 0 & 0 & 0 & 1 & 0 & 0 \\ 0 & 0 & 0 & 0 & 0 & 0 & 1 & 0 \\ 0 & 0 & 0 & 0 & -1 & 0 & 0 & 0 \\ 0 & 0 & 0 & 0 & 0 & 0 & 0 & -1 \end{pmatrix}.$$

We then define

$$w_3=\frac{i}{4\pi}\int_{\mathbb{C}_3}\mathrm{d}\mathbf{k}\cdot\mathrm{Tr}[Q^{-1}(\mathbf{k})D_3\partial_{\mathbf{k}}Q(\mathbf{k})]=\frac{1}{\pi}\int_0^{2\pi}\mathrm{d}k\,\frac{d_1\partial_k d_2-d_2\partial_k d_1}{|d_1|^2+|d_2|^2}, \tag{8}$$

with $D_3=\begin{pmatrix} -3 & 0 & 0 & 0 \\ 0 & 1 & 0 & 0 \\ 0 & 0 & 1 & 0 \\ 0 & 0 & 0 & 1 \end{pmatrix}$. It is required that $-d_1 = d_3 = d_5$ and $d_2 = d_4 = d_6$ when $k_x = -k_y = k_z$.

For the 2π/3 rotation symmetry axes $\mathbb{C}_4$ pointing along the sites 7 and 2, the corresponding 2π/3 rotation symmetry operator $\hat{C}_{3,4}$ leads to $\hat{C}_{3,4}H(k_x,k_y,k_z)\hat{C}_{3,4}^{-1}=H(-k_z,k_x,-k_y)$, which is satisfied when

$$\begin{aligned}
d_1(k_x,k_y,k_z) &\overset{\hat{C}_{3,4}}{=} -d_5(-k_z,k_x,-k_y),\\
d_2(k_x,k_y,k_z) &\overset{\hat{C}_{3,4}}{=} d_6(-k_z,k_x,-k_y),\\
d_3(k_x,k_y,k_z) &\overset{\hat{C}_{3,4}}{=} d_1(-k_z,k_x,-k_y),\\
d_4(k_x,k_y,k_z) &\overset{\hat{C}_{3,4}}{=} d_2(-k_z,k_x,-k_y),\\
d_5(k_x,k_y,k_z) &\overset{\hat{C}_{3,4}}{=} -d_3(-k_z,k_x,-k_y),\\
d_6(k_x,k_y,k_z) &\overset{\hat{C}_{3,4}}{=} d_4(-k_z,k_x,-k_y),
\end{aligned}$$

where

$$\widehat{C}_{3,4}=\begin{pmatrix} 0&0&1&0&0&0&0&0\\ 0&1&0&0&0&0&0&0\\ 0&0&0&1&0&0&0&0\\ 1&0&0&0&0&0&0&0\\ 0&0&0&0&0&0&0&-1\\ 0&0&0&0&1&0&0&0\\ 0&0&0&0&0&0&1&0\\ 0&0&0&0&0&-1&0&0 \end{pmatrix}.$$

We then define

$$w_3=\frac{i}{4\pi}\int_{\mathbb{C}_3}\mathrm{d}\mathbf{k}\cdot\mathrm{Tr}[Q^{-1}(\mathbf{k})D_3\partial_{\mathbf{k}}Q(\mathbf{k})]=\frac{1}{\pi}\int_0^{2\pi}\mathrm{d}k\,\frac{d_1\partial_k d_2-d_2\partial_k d_1}{|d_1|^2+|d_2|^2},\tag{9}$$

with $D_3=\begin{pmatrix} -3&0&0&0\\ 0&1&0&0\\ 0&0&1&0\\ 0&0&0&1 \end{pmatrix}$. It is required that $d_1=d_3=-d_5$ and $d_2=d_4=d_6$ when $k_x=k_y=-k_z$.

In the following, we explain the connection between the winding number and the Wilson loop matrix. Using the form of (3), we can give the expression of the Berry connection with $A_i^{\alpha\beta}=i\left\langle\psi_k^\alpha\middle|\partial_{k_i}\middle|\psi_k^\beta\right\rangle$. We first get that

$$\begin{aligned} A_x^{11}&=i\langle\psi_1|\partial_{k_x}|\psi_1\rangle=\frac{1}{2\varepsilon^2}\left(-d_3\partial_{k_x}d_4+d_4\partial_{k_x}d_3\right),\\ A_y^{11}&=i\langle\psi_1|\partial_{k_y}|\psi_1\rangle=\frac{1}{2\varepsilon^2}\left(d_1\partial_{k_y}d_2-d_2\partial_{k_y}d_1\right),\\ A_z^{11}&=i\langle\psi_1|\partial_{k_z}|\psi_1\rangle=\frac{1}{2\varepsilon^2}\left(-d_5\partial_{k_z}d_6+d_6\partial_{k_z}d_5\right). \end{aligned}\tag{10}$$

We therefore find that along path $\mathbb{C}_1$, there is

$$\int_{\mathbb{C}_1}\left(A_x^{11}\mathrm{d}k_x+A_y^{11}\mathrm{d}k_y+A_z^{11}\mathrm{d}k_z\right)=-\frac{1}{6}\int_{\mathbb{C}_1}\frac{d_1\partial_{k_y}d_2-d_2\partial_{k_y}d_1}{|\tilde{\mathbf{d}}|^2}=-\frac{\pi}{6}w_1.\tag{11}$$

We can also get that

$$\begin{aligned}
A_x^{12} &= i\langle\psi_1|\partial_{k_x}|\psi_2\rangle = 0,\\
A_y^{12} &= i\langle\psi_1|\partial_{k_y}|\psi_1\rangle = \frac{1}{2\varepsilon^2}\left(-d_5\partial_{k_y}d_2 + d_6\partial_{k_y}d_1 + id_6\partial_{k_y}d_2 + id_5\partial_{k_y}d_1\right),\\
A_z^{12} &= i\langle\psi_1|\partial_{k_z}|\psi_1\rangle = \frac{1}{2\varepsilon^2}\left(-d_1\partial_{k_z}d_6 + d_2\partial_{k_z}d_5 - id_2\partial_{k_z}d_6 - id_1\partial_{k_z}d_5\right).
\end{aligned} \tag{12}$$

We find that

$$\int_{\mathbb{C}_1}\left(A_x^{12}\mathrm{d}k_x + A_y^{12}\mathrm{d}k_y + A_z^{12}\mathrm{d}k_z\right) = -\frac{1}{3}\int_{\mathbb{C}_1}\frac{d_1\partial_{k_y}d_2 - d_2\partial_{k_y}d_1}{|\tilde{\mathbf{d}}|^2} = -\frac{\pi}{3}w_1. \tag{13}$$

Other components of the Berry connection can be calculated as well, and we finally conclude that along path $\mathbb{C}_1$, there is

$$\int_{\mathbb{C}_1}\mathbf{A}\cdot\mathrm{d}\mathbf{k} = \frac{\pi}{2}w_1M_1, \tag{14}$$

where

$$M_1 = \begin{pmatrix} -1/3 & -2/3 & 0 & 2/3 \\ -2/3 & -1/3 & 0 & -2/3 \\ 0 & 0 & 1 & 0 \\ 2/3 & -2/3 & 0 & -1/3 \end{pmatrix}.$$

For other paths along $\mathbb{C}_2$, $\mathbb{C}_3$, and $\mathbb{C}_4$, the connection between the winding number and the Wilson loop matrix is found as

$$W_{\mathbb{C}_i} = \exp\left(i(\pi/2)w_iM_i\right), \tag{15}$$

where

$$M_2 = \begin{pmatrix} 1/3 & 1/3 & -2/3 & 0 \\ -2/3 & 1/3 & -2/3 & 0 \\ -2/3 & -2/3 & 1/3 & 0 \\ 0 & 0 & 0 & -1 \end{pmatrix}, M_3 = \begin{pmatrix} -1 & 0 & 0 & 0 \\ 0 & 1/3 & 2/3 & -2/3 \\ 0 & 2/3 & 1/3 & 2/3 \\ 0 & -2/3 & 2/3 & 1/3 \end{pmatrix}, M_4 = \begin{pmatrix} 1/3 & 0 & 2/3 & 2/3 \\ 0 & -1 & 0 & 0 \\ 2/3 & 0 & 1/3 & -2/3 \\ 2/3 & 0 & -2/3 & 1/3 \end{pmatrix},$$

are for path $\mathbb{C}_2$, $\mathbb{C}_3$, and $\mathbb{C}_4$, respectively.

Supplementary Note 2. The synchronization between real-space motion and band-population dynamics.

In this section, we give an elucidation on the synchronization between real-space and band-population dynamics with the atomic limit $J_2 = 0$, where we study the time dynamics of a single unit sell. Now the lowest energy eigenstates are

$$\begin{aligned}
\left|\psi^1\right\rangle &= \left(0, 1/\sqrt{6}, 1/\sqrt{6}, -1/\sqrt{6}, 0, 0, 0, 1/\sqrt{2}\right)^T, \\
\left|\psi^2\right\rangle &= \left(-1/\sqrt{6}, 0, -1/\sqrt{6}, -1/\sqrt{6}, 0, 0, 1/\sqrt{2}, 0\right)^T, \\
\left|\psi^3\right\rangle &= \left(1/\sqrt{6}, -1/\sqrt{6}, 0, -1/\sqrt{6}, 0, 1/\sqrt{2}, 0, 0\right)^T, \\
\left|\psi^4\right\rangle &= \left(-1/\sqrt{6}, -1/\sqrt{6}, 1/\sqrt{6}, 0, 1/\sqrt{2}, 0, 0, 0\right)^T.
\end{aligned} \tag{16}$$

By setting the spatial origin at the plaquette center we can construct the position operator $\hat{\mathbf{r}} = \sum_i \left(\mathbf{r}_i - \mathbf{r}_0\right) \left|\mathbf{r}_i\right\rangle \left\langle \mathbf{r}_i\right|$,whose components on three directions are the matrices

$$\begin{aligned}
\hat{x} &= \mathrm{diag}\left(-1/2, -1/2, 1/2, 1/2, -1/2, -1/2, 1/2, 1/2\right)\delta, \\
\hat{y} &= \mathrm{diag}\left(1/2, -1/2, 1/2, -1/2, 1/2, -1/2, 1/2, -1/2\right)\delta, \\
\hat{z} &= \mathrm{diag}\left(-1/2, 1/2, 1/2, -1/2, 1/2, -1/2, -1/2, 1/2\right)\delta.
\end{aligned} \tag{17}$$

Then we construct the projected position operators $\hat{r}_{P,i} = \hat{P}\hat{r}_i\hat{P} = \sum_{\alpha,\beta=1}^{4} \left|\psi^\alpha\right\rangle \left\langle \psi^\alpha\right| \hat{r}_i \left|\psi^\beta\right\rangle \left\langle \psi^\beta\right|$ for $i = x, y, z$, with $\hat{P} = \sum_{\alpha=1}^{4} \left|\psi^\alpha\right\rangle \left\langle \psi^\alpha\right|$. Notice that there is $\left[\hat{r}_i, \hat{r}_j\right] \neq 0$ when $i \neq j$. Given an applied force $\mathbf{F}$, the perturbative Hamiltonian governing the dynamics reads

$$\begin{aligned}
\hat{H}_F &= \mathbf{F}\cdot\hat{\mathbf{r}}_P = \sum\nolimits_{i=x,y,z} F_i \hat{r}_{P,i} \\
&= \frac{\delta}{3}\begin{pmatrix}
F_x - F_y + F_z & \left(-F_y - F_z\right)/2 & \left(F_x - F_z\right)/2 & \left(F_x + F_y\right)/2 \\
\left(-F_y - F_z\right)/2 & F_x + F_y - F_z & \left(F_x - F_y\right)/2 & \left(-F_x - F_z\right)/2 \\
\left(F_x - F_z\right)/2 & \left(F_x - F_y\right)/2 & -F_x - F_y - F_z & \left(-F_y + F_z\right)/2 \\
\left(F_x + F_y\right)/2 & \left(-F_x - F_z\right)/2 & \left(-F_y + F_z\right)/2 & -F_x + F_y + F_z
\end{pmatrix}.
\end{aligned} \tag{18}$$

Starting with the initial state $\left|\psi_{\mathbf{k}}(0)\right\rangle = \eta_1(0)\left|\psi_{\mathbf{k}}^1\right\rangle + \eta_2(0)\left|\psi_{\mathbf{k}}^2\right\rangle + \eta_3(0)\left|\psi_{\mathbf{k}}^3\right\rangle + \eta_4(0)\left|\psi_{\mathbf{k}}^4\right\rangle$, the evolution results of the wavepacket can be expressed as the solution of the Schrodinger's equation as $\left|\psi_{\mathbf{k}}(t)\right\rangle = U(t)\left|\psi_{\mathbf{k}}(0)\right\rangle$, where the evolution operator reads $U(t) = e^{-i\hat{H}_F t}$. Let us focus on the dynamics along path $\mathbb{C}_1$, where $F_x = F_y = F_z$. The evolution operator can be expressed as

$$U_{\mathbb{C}_1}(t)=\frac{1}{3}\begin{pmatrix} 2+e^{-i\delta F_x t} & 1-e^{-i\delta F_x t} & 0 & -1+e^{-i\delta F_x t} \\ 1-e^{-i\delta F_x t} & 2+e^{-i\delta F_x t} & 0 & 1-e^{-i\delta F_x t} \\ 0 & 0 & 3e^{i\delta F_x t} & 0 \\ -1+e^{-i\delta F_x t} & 1-e^{-i\delta F_x t} & 0 & -1+e^{-i\delta F_x t} \end{pmatrix}. \tag{19}$$

We can calculate the time-dependent coefficients $\eta_i(t)$ as

$$\begin{aligned} \eta_1(t) &= \frac{1}{3}[2\eta_1(0)+\eta_2(0)-\eta_4(0)+e^{-i\delta F_x t}(\eta_1(0)-\eta_2(0)+\eta_4(0))], \\ \eta_2(t) &= \frac{1}{3}[\eta_1(0)+2\eta_2(0)-\eta_4(0)+e^{-i\delta F_x t}(-\eta_1(0)+\eta_2(0)-\eta_4(0))], \\ \eta_3(t) &= e^{i\delta F_x t}\eta_3(0), \\ \eta_4(t) &= \frac{1}{3}[-\eta_1(0)+\eta_2(0+2\eta_4(0))+e^{-i\delta F_x t}(\eta_1(0)-\eta_2(0)+\eta_4(0))]. \end{aligned} \tag{20}$$

It can be seen that the band populations can be expressed as

$$\left|\eta_i(t)\right|^2 = M_i^2+N_i^2+2M_iN_i\cos(\delta F_x t), \tag{21}$$

for i = 1, 2, 4, where M_i and N_i are constant coefficients consisting of $\eta_1(0)$, $\eta_2(0)$, and $\eta_4(0)$. As a result, the band populations $\left|\eta_i(t)\right|^2$ experience cosine oscillations with a period $2\pi/\left(\delta\left|F_x\right|\right)$ except for $\left|\eta_3(t)\right|^2$, which remains unchanged. Meanwhile, the period for the BO along the body diagonal is $T_B=\left|\mathbf{G}\right|/\left|\mathbf{F}\right|=\pi/\left(\delta\left|F_x\right|\right)$, which is half of that for the band-population dynamics. The synchronization along the other three paths can also be demonstrated.

Supplementary Note 3. The influence of non-abelian Berry curvature on real-space dynamics

In this section, we analyze the influence of non-Abelian Berry curvature on the motion of the center-of mass of the wavepacket in real space. The center-of mass of the real space wavepacket satisfies the semiclassical equation as

$$\dot{\mathbf{r}}=\partial_{\mathbf{k}}\varepsilon(\mathbf{k})-\dot{\mathbf{k}}\times\eta^{\dagger}\mathbf{B}\eta, \tag{22}$$

which has three components in 3D space,

$$
\begin{aligned}
\dot{x} &= \partial_{k_x}\varepsilon - (F_y\eta^\dagger B_z\eta - F_z\eta^\dagger B_y\eta),\\
\dot{y} &= \partial_{k_y}\varepsilon - (F_z\eta^\dagger B_x\eta - F_x\eta^\dagger B_z\eta),\\
\dot{z} &= \partial_{k_z}\varepsilon - (F_x\eta^\dagger B_y\eta - F_y\eta^\dagger B_x\eta),
\end{aligned}
\tag{23}
$$

where

$$
\begin{aligned}
B_x &= \partial_{k_y}A_z - \partial_{k_z}A_y - i\left[A_y, A_z\right],\\
B_y &= \partial_{k_z}A_x - \partial_{k_x}A_z - i\left[A_z, A_x\right],\\
B_z &= \partial_{k_x}A_y - \partial_{k_y}A_x - i\left[A_x, A_y\right],
\end{aligned}
\tag{24}
$$

are the components of the non-Abelian Berry curvature $\mathbf{B} = \nabla_k \times \mathbf{A} - i\mathbf{A}\times\mathbf{A}$. Now we take path $\mathbb{C}_1$ for example, where the applied force $\mathbf{F} = (F_x, F_y, F_z)$ satisfies $F_x = F_y = F_z$, which leads to $k_x = k_y = k_z = k$ (we assume that we start with $\mathbf{k}_0 = 0$ and thus $\mathbf{k}_t = \mathbf{F}t$). We can write the Berry curvature as

$$
\begin{aligned}
B_x &= \frac{1}{8\varepsilon^4}\begin{pmatrix}
-4\Delta\mu_k & -i\left(3\Delta^2+4\mu_k^2\right) & -2\gamma_k^*\mu_k & -2\Delta\mu_k-4i\mu_k^2\\
i\left(3\Delta^2+4\mu_k^2\right) & 4\Delta\mu_k & 2\gamma_k^*\mu_k & -2\Delta\mu_k-4i\mu_k^2\\
-2\gamma_k\mu_k & 2\gamma_k\mu_k & 0 & -2\gamma_k\mu_k+3i\Delta\gamma_k\\
-2\Delta\mu_k+4i\mu_k^2 & -2\Delta\mu_k-4i\mu_k^2 & -2\gamma_k^*\mu_k-3i\Delta\gamma_k^* & 0
\end{pmatrix},\\
B_y &= \frac{1}{8\varepsilon^4}\begin{pmatrix}
0 & 2\Delta\mu_k-4i\mu_k^2 & -2\gamma_k\mu_k-3i\Delta\gamma_k & 2\Delta\mu_k-4i\mu_k^2\\
2\Delta\mu_k+4i\mu_k^2 & -4\Delta\mu_k & 2\gamma_k^*\mu_k & -i\left(3\Delta^2+4\mu_k^2\right)\\
-2\gamma_k^*\mu_k+3i\Delta\gamma_k^* & 2\gamma_k\mu_k & 0 & -2\gamma_k\mu_k\\
2\Delta\mu_k+4i\mu_k^2 & i\left(3\Delta^2+4\mu_k^2\right) & -2\gamma_k^*\mu_k & 4\Delta\mu_k
\end{pmatrix},\\
B_z &= \frac{1}{8\varepsilon^4}\begin{pmatrix}
4\Delta\mu_k & -2\Delta\mu_k-4i\mu_k^2 & -2\gamma_k^*\mu_k & -i\left(3\Delta^2+4\mu_k^2\right)\\
-2\Delta\mu_k+4i\mu_k^2 & 0 & 2\gamma_k^*\mu_k+3i\Delta\gamma_k^* & 2\Delta\mu_k-4i\mu_k^2\\
-2\gamma_k\mu_k & 2\gamma_k\mu_k-3i\Delta\gamma_k & 0 & -2\gamma_k\mu_k\\
i\left(3\Delta^2+4\mu_k^2\right) & 2\Delta\mu_k+4i\mu_k^2 & -2\gamma_k^*\mu_k & -4\Delta\mu_k
\end{pmatrix},
\end{aligned}
\tag{25}
$$

where $\Delta = J_1^2 - J_2^2, \mu_k = J_1J_2\sin(k),$ and $\gamma_k = e^{ik}J_1^2 - e^{-ik}J_2^2.$

The velocity equation (22) contains two parts, as $\dot{\mathbf{r}} = \dot{\mathbf{r}}_\parallel + \dot{\mathbf{r}}_\perp$. The first term of the right can be represented as $\dot{\mathbf{r}}_\parallel = \partial_\mathbf{k}\varepsilon(\mathbf{k}) = -J_1J_2\sin\left(\mathbf{k}\right)/\varepsilon$, which is parallel to the force $\mathbf{F}$. The second term is $\dot{\mathbf{r}}_\perp = -\dot{\mathbf{k}} \times \eta^\dagger \mathbf{B} \eta = F_x \left(\eta^\dagger \left(B_y - B_z \right) \eta, \eta^\dagger \left(B_z - B_x \right) \eta, \eta^\dagger \left(B_x - B_y \right) \eta \right)$, which is obviously perpendicular to **F** and leads to the transverse Hall drift.

Now we discuss the period of the Hall motion caused by the non-Abelian Berry curvature. According to the equation

$$\eta(t) = \exp\left(-i \int_0^t \varepsilon(\mathbf{k}) \mathrm{d}t\right) W \eta(0), \tag{26}$$

and the results of W calculated in Supplementary Note 1, we find that η is a periodic function of k and the period is 4π (the overall phase is ignored). Moreover, the period of **B** is 2π. Thus, we can infer that $\dot{\mathbf{r}}_\perp = -\dot{\mathbf{k}} \times \eta^\dagger \mathbf{B} \eta$ is periodic about k and the period is 4π. We can further obtain the relationship $W_{\mathbb{C}_1}^\dagger \mathbf{B} W_{\mathbb{C}_1} = -\mathbf{B}$ using the results in (15) and (25), which results in the equation $\dot{\mathbf{r}}_\perp(k + 2\pi) = -\dot{\mathbf{r}}_\perp(k)$. This is indicated that the Hall velocity in the second BO ($2\pi < k < 4\pi$) will be exactly opposite to that in the first one, and the accumulated Hall displacement is offset during two BOs. In conclusion, the transverse Hall drift of the center-of mass has a period of $2T_B$.

We can numerically display the evolution of the velocity as shown in Fig. S2(a). Figure S2(a) illustrates the evolution of the components of velocities $\dot{\mathbf{r}}_{\parallel}$ and $\dot{\mathbf{r}}_\perp$ on x direction $\dot{x}_{\parallel}$ and $\dot{x}_\perp$, respectively. It can be seen that in $0 < t < T_B/2$, $\dot{x}_{\parallel}$ is positive and $\dot{x}_\perp$ is negative, and $\dot{x}_{\parallel}$ changes the sign at $t = T_B/2$, where the longitudinal displacement of the center-of mass reaches the maximum. In $T_B/2 < t < T_B$, $\dot{x}_{\parallel}$ and $\dot{x}_\perp$ are both negative, thus the longitudinal displacement starts reducing and the transverse displacement continues growing. The latter reaches the maximum at $t = T_B$. In the second BO, the longitudinal displacement repeats while the transverse velocity changes the sign and bring the center-of mass to its initial position at $t = 2T_B$.

To validate the semiclassical real-space dynamics, we also numerically simulate the evolution of a real-space wavepacket using a finite size lattice consisting of $N_x \times N_y \times N_z$ unit cells. The initial state is a Gaussian wavepacket centered at $\mathbf{k}_0 = \Gamma$ of the form

$$\left|\psi_{\mathbf{r},\mu}(t=0)\right\rangle = \sum_{\mathbf{k}} e^{-k^2/2\sigma^2} e^{i\mathbf{k}\cdot(\mathbf{r}_\mu - \mathbf{r}_0)} \left|\psi_{\mathbf{k},\mu}(0)\right\rangle,$$

where μ indicates the sublattice degree of freedom in the unit cell and $\mathbf{r}_\mu$ is its spatial position. We take a grid of $N_x \times N_y \times N_z$ points in $\mathbf{k}$ space within an interval $\mathbf{k} \in [-3\sigma, 3\sigma] \times [-3\sigma, 3\sigma] \times [-3\sigma, 3\sigma]$. We evolve the state with the real-space Hamiltonian H_B and calculate the observable $\mathbf{r}^{\mathrm{num}}(t) = \langle \psi(t)|\hat{\mathbf{r}}|\psi(t)\rangle$ with $\hat{\mathbf{r}} = \sum_i (\mathbf{r}_i - \mathbf{r}_0)|\mathbf{r}_i\rangle\langle\mathbf{r}_i|$. Figure S2(b) shows the simulation results of the wavepacket's evolution on x direction, marked by red dots. Here, $N_i = 15$, $F_i = -0.4J_1$ for $i = x, y, z$, and $\sigma = 0.15a^{-1}$. The spatial trajectory is given in Fig. S2(c). It is clearly seen that the numerical results match the semiclassical results (blue curves) well.

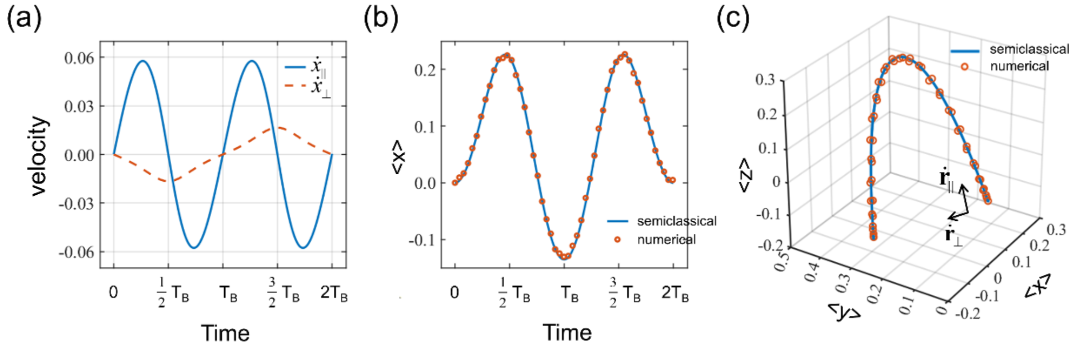

Figure S2. The transverse Hall drift caused by the non-Abelian Berry curvature. (a) Longitudinal (blue solid line) and transverse (red dashed line) velocities on x direction represented by $\dot{x}_{\parallel}$ and $\dot{x}_{\perp}$, respectively. Their periods are T_B and $2T_B$, respectively. Here $F_x = F_y = F_z = -0.4J_1$ and $J_2 = 0.1J_1$. Thus, $T_B = 5\pi J_1$. (b) Comparison of the wavepacket x position for semiclassical evolution (solid line) and numerical real-space evolution (dots) of a wavepacket with width $\sigma = 0.15\delta^{-1}$. (c) Real-space trajectories.

Supplementary Note 4. Results of the dynamics in paths $\mathbb{C}_2$, $\mathbb{C}_3$, and $\mathbb{C}_4$.

In this section, we illustrate the topological BOs along paths $\mathbb{C}_2$, $\mathbb{C}_3$, and $\mathbb{C}_4$ without providing more proofs. The periodic band population dynamics are shown in Fig. S3(a), (c), and (e), while the spatial trajectories in real space are given in Fig. S3(b), (d), and (f), for paths

$\mathbb{C}_2$, $\mathbb{C}_3$, and $\mathbb{C}_4$, respectively. For path $\mathbb{C}_2$, we take an applied force of $-F_x = F_y = F_z = -0.4J_1$ and the initial distribution of $\eta(0) = (1,0,0,0)^T$. For path $\mathbb{C}_2$, we take an applied force of $F_x = -F_y = F_z = -0.4J_1$ and the initial distribution of $\eta(0) = (0,1,0,0)^T$. For path $\mathbb{C}_2$, we take an applied force of $F_x = F_y = -F_z = -0.4J_1$ and the initial distribution of $\eta(0) = (1,0,0,0)^T$. The double-period evolution of both the band population dynamics and the transverse Hall drifts can clearly be seen from the figures.

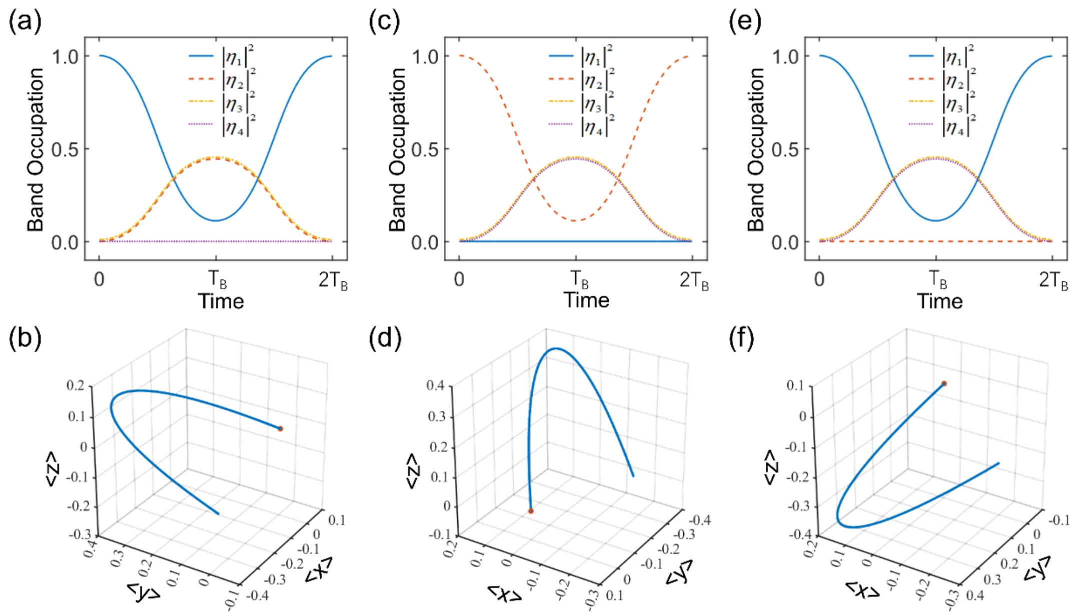

Figure S3. The results under paths $\mathbb{C}_2$, $\mathbb{C}_3$, **and** $\mathbb{C}_4$. (a), (b) Band occupation dynamics and Real-space trajectories under path $\mathbb{C}_2$ with initial distribution of $\eta(0) = (1,0,0,0)^T$. (c), (d) Band occupation dynamics and Real-space trajectories under path $\mathbb{C}_3$ with initial distribution of $\eta(0) = (0,1,0,0)^T$. (e), (f) Band occupation dynamics and Real-space trajectories under path $\mathbb{C}_4$ with initial distribution of $\eta(0) = (1,0,0,0)^T$.

Supplementary Note 5. Details for the Experimental realization of 3D non-Abelian BOs.

In this section, we give more details on the experimental realization of the topological BOs.

A circuit network with 3D structure is built as shown in Fig. S4(a), which consists of $3\times3\times3$ unit cells. The circuit network is composed of modular designed small PCBs spliced together. Figure S4(b) illustrates the connection of two lattice sites A and B represented by two pairs of circuit nodes through two kinds of PCB modules i (iii) and ii. Here, the left and right parts of module i constitute the real nodes of A and B, respectively. While the left and right parts of module iii constitute the imaginary nodes. They are cross-connected via two INICs provided by module ii, which is indicated by orange lines in Fig. S4(b). The key components are marked in the diagram. The grounding capacitors are 1 μF thin film capacitors. The resistors are surface-mounted device (SMD) resistors with the 0603 package. All values of the capacitors and resistors are manually selected to within a tolerance of 1% to the theoretical values. For the realization of the INIC, we use the precision dual operational amplifier LT1013 (Linear Technology), which has a large signal voltage gain. The two feedback resistors of the INIC are chosen to have the same value to the effective one. Moreover, the modules are connected through contact pins and wires with very small resistances (less than 10 mΩ), which helps to reduce the influence of the parasitic effects.

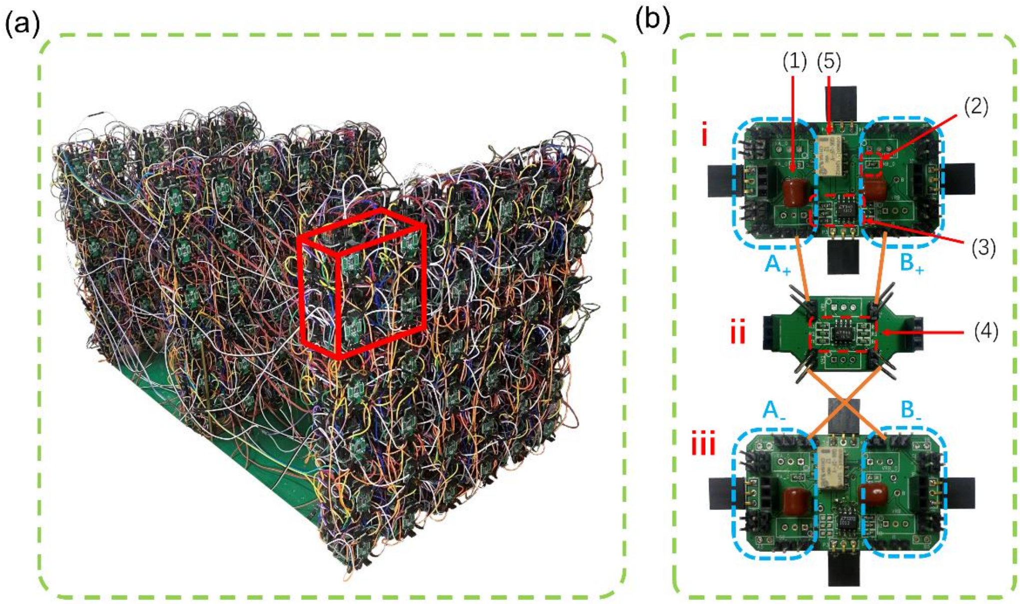

Figure S4. Photograph images of the designed circuits for topological BOs. (a) A photo of the 3D circuit network consisting of $3\times3\times3$ unit cells. One unit cell is indicated by the red box. (b) Two kinds of PCB modules in the circuits. The numbers label some important components.

(1) The grounding capacitor for node A_+. (2) The grounding resistor for node B_+. (3) The grounding INIC for node A_+. (4) Connecting INICs for sites A and B. (5) A relay controlling the initial signals.

At the beginning of the experiments, all the nodes are connected to external signals provided by DC power sources to match the initial circuit states. We use relay model G6K (Omron) to connect the nodes and the external signals. The relays are controlled by a signal of 12 V through a mechanical switch. With this setting, the external signals can be removed at the same time. The measured quantities of our circuit are the evolving voltages at all nodes. Thus, we connect the nodes to an oscilloscope by coaxial cables and measure the voltages at all time. We use a 4-channel oscilloscope DSO7104B (Agilent Technologies) in our experiments to collect voltage data. The measurements are repeated for at least 10 times to verify the reproducibility of the obtained results.

Supplementary Note 6. The influence of disorder effects on the Bloch oscillations in circuit simulators.

In the main text, we have numerically simulated the topological BOs in our designed circuit with ideal circuit components. However, under real experimental conditions, circuit components inevitably have errors, which affects the accuracy of experimental results. In this part, we numerically investigated the influence of disorder effects on the BOs and the band population dynamics in circuits. As shown in Fig. S5(a), the evolution of the center-of mass of the circuit wavepacket on x direction with different fluctuations of circuit elements (0%, 1%, 3% and 5%) are presented. The spatial trajectories are shown in Fig. S5(b). Here, the values of the fluctuations represent how much the disorder can be to the ideal values in both capacitances and resistances. We can see that the double period of BOs is still maintained with the small disorder strength. While, when the disorder strength approaches to 3%, there is a significant attenuation in the second BO of the circuit wavepacket. When the disorder strength approaches to 5%, the BOs are destroyed.

Moreover, the band population dynamics under disorders are also studied by transforming the real-space wavepacket into momentum space using the inverse Fourier transform, namely,

$$\left|\psi_{\mathbf{k},\mu}(t)\right\rangle = \frac{1}{\sqrt{N}}\sum_{\mathbf{r}} e^{-i\mathbf{k}(t)\cdot(\mathbf{r}_\mu-\mathbf{r}_0)}\left|\psi_{\mathbf{r},\mu}(t)\right\rangle . \tag{27}$$

The evolution results with different disorder strengths are displayed in Fig. S5(c). It can be seen that the band occupations are broken when the disorder strength reaches to 3%, which is consistent with the BO behavior in Fig. S5(a) and (b).

It is worthy to note that in addition to the disorders of circuit components, there are other instabilities in realistic circuits that can affect the accuracy of experimental results. For example, the parasitic effects, especially the parasitic resistances, that exist in circuit components and PCBs will break the hermiticity of the circuit Hamiltonian, which leads to the decay of the voltage signals in the circuit evolution. Moreover, delays of the signals and errors in measurements may also affect the experimental results. Some of these instabilities can be reduced by appropriate experimental settings, as we have discussed in the former section.

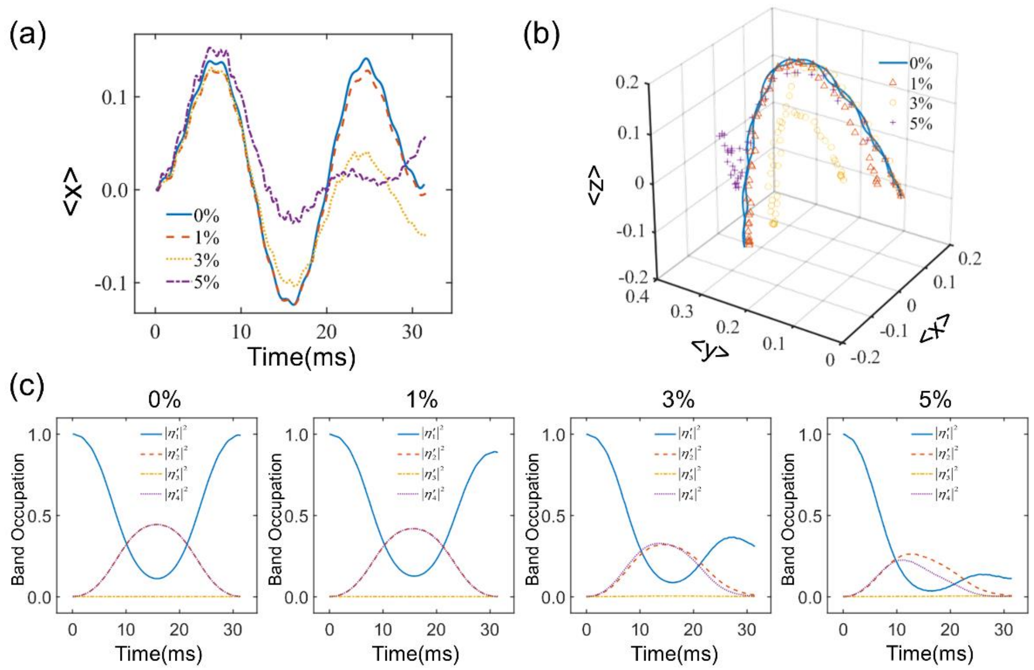

Figure S5. Numerical results for the influences of disorder effects. (a) The evolution of real-space center-of mass on x direction with fluctuations of circuit components being 0%, 1%, 3%, and 5%. (b) Spatial trajectories. (c) The band population dynamics with fluctuations of circuit components being 0%, 1%, 3%, and 5%.

Supplementary Note 7. Topologically protected 2D surface states.

As has been mentioned in the main text, there are not only 1D edge states that localized on the hinges of the system, but also 2D boundary states that localized on the surfaces. Here we give an example. Figure S6(a) shows the numerically calculated eigenvalues of a 6×6×6 unit-cell system with periodic boundary conditions along z' direction and open boundary conditions along x' and y' directions. The eigenstates with different kinds of distributions are marked by different colors. Figure S6(b) illustrates the distribution of an example for the states marked by blue in Fig. S6(a). It is clearly seen that the density of the state is well localized at the surfaces of the system, except for the hinges. We note that the surface states are also topologically protected, which means they only exist when $J_2 > J_1$.

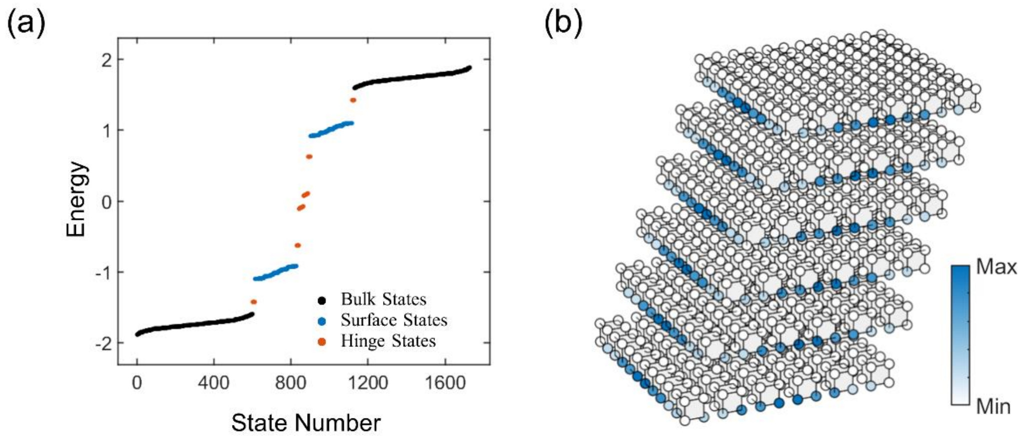

Figure S6. Topologically protected 2D surface states. (a) Eigenvalues of a 6×6×6 unit-cell system with three different kinds of distributions. (b) An example for the topologically protected 2D surface states.

Supplementary Note 8. The proof for the topological properties of novel higher-order 1D boundary states.

In previous works, Benalcazar *et al.* have introduced a class of HOTIs hosting higher bulk multipole moments, whose nontrivial nature leads to topologically protected corner charges. This bulk-boundary correspondence has been expressed in terms of a topological invariant computed using the eigenstates of the Wilson loop operator, dubbed the "nested Wilson loop" procedure to reveal the corner modes. We take the 2D BBH model as example for a brief introduction. Consider the Wilson loop in x direction

$$\mathcal{W}_{x,k} = F_{x,k+N_x\Delta k_x} \cdots F_{x,k+\Delta k_x} F_{x,k}, \tag{28}$$

where $\left[F_{x,k}\right]^{mn} = \left\langle u^m_{k+\Delta k_x} \middle| u^n_k \right\rangle$ with $\left|u^n_k\right\rangle$ being the occupied energy bands. With fully periodic boundary conditions, the Wilson loop for our model diagonalizes as

$$\mathcal{W}_{x,k} = \sum_{j=\pm} \left|v^j_{x,k}\right\rangle e^{2\pi i v^j_x(k_y)} \left\langle v^j_{x,k}\right|, \tag{29}$$

where the eigenstates $\left|v^j_{x,k}\right\rangle$, $j = 1, 2$, have components $\left[v^j_{x,k}\right]^n$, $n = 1, 2$. Defining the Wannier band subspaces

$$\left|w^\pm_{x,k}\right\rangle = \sum_{n=1,2} \left|u^n_k\right\rangle \left[v^\pm_{x,k}\right]^n, \tag{30}$$

the nested Wilson loops along k_y in the Wannier bands $v^\pm_x$ are

$$\tilde{\mathcal{W}}^\pm_{y,k_x} = F^\pm_{y,k+N_y\Delta k_y} \cdots F^\pm_{y,k+\Delta k_y} F^\pm_{y,k}, \tag{31}$$

where $F^\pm_{y,k} = \left\langle w^\pm_{x,k+\Delta k_y} \middle| w^\pm_{x,k} \right\rangle$, and their associated polarizations are

$$\begin{aligned} p^{v^\pm_x}_y &= -\frac{i}{2\pi}\frac{1}{N_x}\sum_{k_x} \mathrm{Log}\left[\tilde{\mathcal{W}}^\pm_{y,k_x}\right] \\ &= \begin{cases} 0, & |J_1| > |J_2|, \\ 1/2, & |J_1| < |J_2|. \end{cases} \end{aligned} \tag{32}$$

The other polarizations $p^{v^\pm_y}_z$ can be got from another order of the calculation for the Wilson loop and is also quantized to 0 or 1/2. The bulk quadrupole moment is defined as

$$q_{xy} = p^{v^-_x}_y p^{v^-_y}_x + p^{v^+_x}_y p^{v^+_y}_x, \tag{33}$$

obtaining a quantized value $q_{xy} = 0$ or 1/2.

The bulk octupole moment in a 3D model can be calculated in a similar way. Two separated Wannier bands $v^\pm_z(k_x, k_y)$ can be got by calculating the Wilson loop along k_z. Based on $v^+_z(k_x, k_y)$, we can further calculate the nested Wilson loop along k_y and get the wannier bands $\eta^\pm_y(k_z)$. Finally, by calculating the nested Wilson loop along k_x based on $\eta^+_y(k_z)$, we get the

Wannier centers $\tilde{\mathcal{W}}_{x,k}^{+z,+y}$ and the associated polarization

$$\begin{aligned} p_x^{+z,+y} &= -\frac{i}{2\pi}\frac{1}{N_y N_z}\sum_{k_y,k_z}\mathrm{Log}\left[\tilde{\mathcal{W}}_{x,k}^{+z,+y}\right] \\ &= \begin{cases} 0, & |J_1|>|J_2|, \\ 1/2, & |J_1|<|J_2|. \end{cases} \end{aligned} \tag{34}$$

Then, the quantized bulk octupole moment o_{xyz} topologically protects the corner states.

However, bulk multipole moments calculated by nested Wilson loops are not always suitable for the characterization of HOTIs, since they require gapped Wannier bands and specific symmetries. Our boundary state located on the body diagonal is one of the examples, where we can not get a quantized bulk octupole moment of 0 or 1/2 after the calculation of the nested Wilson loop. Here, we demonstrate the existence of the topological boundary states by solving the zero-energy modes under an effective theory. Considering the new spatial directions marked by x', y', and z', as have been introduced in the main text, the Hamiltonian now can be written as

$$\begin{aligned} H'(\mathbf{k}') = &J_2\sin(k_{y'})\Gamma_1' + [J_1 + J_2\cos(k_{y'})]\Gamma_2' \\ &+J_2\sin(k_{x'})\Gamma_3' + [J_1 + J_2\cos(k_{x'})]\Gamma_4' \\ &+J_2\sin(k_{z'}-k_{x'}-k_{y'})\Gamma_5' + [J_1 + J_2\cos(k_{z'}-k_{x'}-k_{y'})]\Gamma_6', \end{aligned} \tag{35}$$

which breaks the original symmetries. Here, we use the convention that the lattice points within the unit cell are all sitting in the center of the unit cell. In order to build an effective theory near zero energy, we take $J_2 = (1+m)J_1$, with $|m| \ll 1$. Notice that our system has eigenvalues $E = \pm mJ_1$ when $\mathbf{k}' = (\pi,\pi,\pi)$. We first study the edge states with periodic boundary conditions along y' and z' directions. Expending the Hamiltonian to the second order of k_x at $\mathbf{k}' = (\pi,\pi,\pi)$, we have

$$\begin{aligned} H'_{eff}(k_{x'}) = &[J_1 - J_2]\Gamma_2' - J_2 k_{x'}\Gamma_3' + [J_1 - J_2(1-k_{x'}^2/2)]\Gamma_4' \\ &+J_2 k_{x'}\Gamma_5' + [J_1 - J_2(1-k_{x'}^2/2)]\Gamma_6'. \end{aligned} \tag{36}$$

We now substitute $k_{x'} \to -i\partial_{x'}$ and use $|m| \ll 1$ to solve the equation $H_{eff}\psi = E\psi$ with $E = 0$. We decompose the eigenstate as $\psi(x') = \varphi(x')\chi$, where $\chi = (\chi_1, \chi_2, \cdots, \chi_8)^T$ and take the ansatz $\varphi(x') \propto e^{-tx'}$, then we have the equations

$$
\begin{aligned}
(-m+t-\frac{1}{2}t^2)\chi_5+m\chi_6+(-m-t-\frac{1}{2}t^2)\chi_7&=0,\\
-m\chi_5+(-m-t-\frac{1}{2}t^2)\chi_6+(m+t+\frac{1}{2}t^2)\chi_8&=0,\\
(m-t+\frac{t^2}{2})\chi_5+(-m-t-\frac{t^2}{2})\chi_7+m\chi_8&=0,\\
(-m+t-\frac{t^2}{2})\chi_6-m\chi_7+(-m+t-\frac{t^2}{2})\chi_8&=0,\\
(-m-t-\frac{1}{2}t^2)\chi_1-m\chi_2+(m+t+\frac{1}{2}t^2)\chi_3&=0,\\
m\chi_1+(-m+t-\frac{1}{2}t^2)\chi_2+(-m-t-\frac{1}{2}t^2)\chi_4&=0,\\
(-m+t-\frac{t^2}{2})\chi_1+(-m+t-\frac{t^2}{2})\chi_3-m\chi_4&=0,\\
(m-t+\frac{t^2}{2})\chi_2+m\chi_3+(-m-t-\frac{t^2}{2})\chi_4&=0.
\end{aligned} \tag{37}
$$

To solve the equations, we rewrite the first four equations in Eq. (37) as

$$
\begin{aligned}
\chi_5&=\frac{(m+t+\frac{t^2}{2})(\chi_8-\chi_6)}{m},\\
\chi_6&=\frac{(m-t+\frac{t^2}{2})\chi_5+(m+t+\frac{t^2}{2})\chi_7}{m},\\
\chi_7&=\frac{-(m-t+\frac{t^2}{2})(\chi_6+\chi_8)}{m},\\
\chi_8&=\frac{(m+t+\frac{t^2}{2})\chi_7-(m-t+\frac{t^2}{2})\chi_5}{m}.
\end{aligned} \tag{38}
$$

To ensure the convergence of χ_i, we take the numerators approximately to 0, as $|m|\ll 1$. To satisfy $(m+t+\frac{t^2}{2})(\chi_8-\chi_6)=0$ and $-(m-t+\frac{t^2}{2})(\chi_6+\chi_8)=0$, we first assume that $\chi_6,\chi_8\neq 0$, which makes (i) $m-t+\frac{t^2}{2}=0$ and $\chi_6=\chi_8$, or (ii) $m+t+\frac{t^2}{2}=0$ and $\chi_6=-\chi_8$. For the situation (i), there are two solutions for *t* as $t_{1,2}=1\pm\sqrt{1-2m}\approx 1\pm(1-m)$. We can construct a solution $\varphi(x')=c_1e^{-t_1x'}+c_2e^{-t_2x'}$, which is exponentially localized for *m* > 0 and vanishes at *x′* = 0, namely c1 = -c2. While the situation (ii) does not satisfy these requirements for any value of m. Thus, we take situation (i). Other equations can be satisfied if we take $\chi_5 = \chi_7 = 0$. When $\chi_6 = \chi_8 = 0$, we can take $\chi_7 = 0$ and $\chi_5 \neq 0$ combining $m - t + \frac{t^2}{2} = 0$ to satisfy the equations.

Similarly, there are two forms of solutions for $\chi_1 \sim \chi_4$, that is $\chi_1 = \chi_3 \neq 0, \chi_2 = \chi_4 = 0$ or $\chi_2 \neq 0, \chi_1 = \chi_3 = \chi_4 = 0$. In conclusion, we can give a set of zero-energy solutions as $\psi(x') = \varphi(x')\chi$ where

$$\begin{aligned}
\chi_a &= (0,0,0,0,0,1/\sqrt{2},0,1/\sqrt{2})^T, \\
\chi_b &= (0,0,0,0,1,0,0,0)^T, \\
\chi_c &= (1/\sqrt{2},0,1/\sqrt{2},0,0,0,0,0)^T, \\
\chi_d &= (0,1,0,0,0,0,0,0)^T,
\end{aligned}$$

and $\varphi(x') = e^{-(2-m)x'} - e^{-mx'}$.

These results reflect that there are four zero-energy modes localized at the edge $x' = 0$ that exist only for $m > 0$, namely for $J_2 > J_1$. With a similar method, we can get the zero-energy modes localized at the edge $y' = 0$ with periodic boundary conditions along the x' and z' directions. These boundary modes of the two directions finally lead to the boundary states that are localized at the 1D hinge of the system with open boundary conditions along the x' and y' directions, which is shown in the main text.

Supplementary Note 9. Designed circuits for the topologically protected 1D boundary states.

We illustrate the schematic diagram for the designed circuit for the demonstration of the boundary states, as shown in Fig. S7. As can be seen, the circuit network for the 1D boundary states consists of $3\times3\times3$ unit cells divided into three layers, and is connected end-to-end in the z direction, which is shown by the double-headed black arrows in Fig. S7. Sites within different layers are connected like steps to achieve the open boundaries along the body diagonals. Moreover, there is no INIC between the nodes pair for a site since we do not need an external force. After setting the circuit components appropriately, the evolution of the voltages at each node $a_\pm$ can be written as the differential equations through Kirchhoff's current law, as $C_{a_\pm}\frac{dV_{a_\pm}}{dt}+\frac{V_{a_\pm}}{R_{a_\pm}}=\sum_b \frac{V_{b_\mp}-V_{a_\pm}}{R_{a_\pm b_\mp}}$, which can be written in the form of a Schrödinger-like equation $i\partial_t|\phi(t)\rangle = H_e'|\phi(t)\rangle$, where $|\phi(t)\rangle = (V_{1_+}(t),\cdots,V_{n_+}(t),V_{1_-}(t),\cdots,V_{n_-}(t))^T$ and $H_e' = i\begin{pmatrix} O & -H' \\ H' & O \end{pmatrix}$. Here, n = 216 is the number of the sites, and H' is the real-space Hamiltonian corresponding to Eq. (41). After exciting the outermost two sites of the cell located on the hinge, as highlighted in green color in Fig. S7, the evolution results for the circuit satisfy $|\psi(t)\rangle = \left(V_{1+}(t)-iV_{1-}(t),\cdots,V_{n+}(t)-iV_{n-}(t)\right)^T$, and the density of states $|\psi(t)|^2$ can be calculated. The experimental results have been shown in the main text.

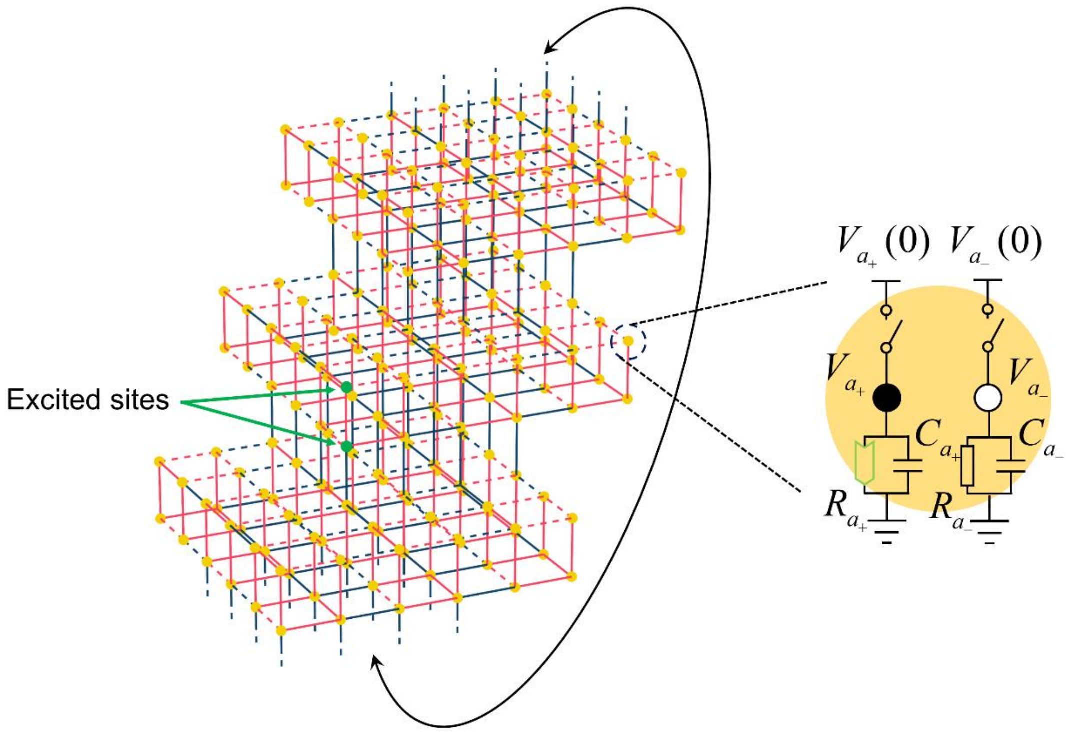

Figure S7. A schematic diagram of the designed circuit for the observation of the 1D boundary states. The circuit network for the 1D boundary state. The circuit site consisting of two nodes is illustrated by the yellow circle. The two sites excited for the initial state are highlighted with the green color.